Fusion Engineering and Design 208 (2024) 114671

Contents lists available at ScienceDirect

Fusion Engineering and Design

journal homepage: www.elsevier.com/locate/fusengdes

First operation and validation of simulations for the divertor cryo-vacuum pump in Wendelstein 7-X

V. Haak [a,*], C.P. Dhard [a], D. Boeyaert [b], T. Bräuer [a], V. Bykov [a], C. Day [c], S. Degenkolbe [a], G. Ehrke [a], J. Igitkhanov [c], M. Khokhlov [a], T. Kremeyer [a], M. Nagel [a], D. Naujoks [a], M. Pietsch [a], D. Pilopp [a], G. Schlisio [a], H. Strobel [c], C. Tantos [c], S. Varoutis [c], H. Viebke [a], O. Volzke [a], W7-X Team [1]

[a] Max–Planck-Institut für Plasmaphysik, 17491, Greifswald, Germany
[b] University of Wisconsin-Madison, Madison, WI, USA
[c] Karlsruhe Institute of Technology, 76344, Eggenstein-Leopoldshafen, Germany

ARTICLE INFO

Keywords:
Cryo-vacuum pumping
Particle exhaust
Divertor neutral gas pressure
Stellarator Wendelstein 7-X

ABSTRACT

Ten cryo-vacuum pumps (CVPs) were installed in the subdivertor region of each island divertor in the stellarator Wendelstein 7-X (W7-X) and operated for the first time during the recently completed plasma campaign OP2.1. A pumping speed of 70 ± 1 $\frac{m^3}{s}$ was measured during dedicated tests with known hydrogen gas injection. Based on a conductance model, the estimated pumping speed ranges from 86-93 $\frac{m^3}{s}$ for different sticking coefficients between 0.6 and 0.8. After completion of the initial tests the CVPs were operated successfully throughout the campaign, with regeneration performed once a week. Neutral gas pressures in the subdivertor in the range of 10^{-4} mbar are well within the molecular flow regime and limit the particle exhaust capabilities of the CVPs. Simulations of the neutral gas pressure in the three-dimensional complex geometry of the subdivertor were performed using the DIVGAS code based on the direct simulation Monte Carlo method and a model implemented in the steady-state thermal package in ANSYS, which are in agreement with the measured values during plasma operation.

1. Introduction

Density control is a necessary requirement for stable operation of a fusion device and is realized by controlled fueling as well as sufficient particle exhaust and recycling. Excessive release of particles from the walls of the plasma vessel creates difficulties in controlling the plasma density by means of gas injection and can ultimately lead to plasma collapse if the released gas cannot be exhausted or recycled. For an optimized magnetic field configuration, in addition to the design of the divertor and other first wall components i.e. baffles, toroidal/poloidal closures which help guide the particles to the subdivertor region, providing an efficient pumping system is an essential requirement for gas exhaust. Due to the limited availability of plasma vessel ports, the mechanical pumping systems can only provide limited pumping capacity. An in-vessel cryo-vacuum pump with high pumping speed helps to significantly increase the pumping in the subdivertor region. This has been implemented in the ASDEX Upgrade [1–4], JET [5], DIII-D [6], KSTAR [7], EAST [8] tokamaks and the LHD stellarator [9,10] and is planned for ITER [11,12]. To increase the pumping capacity and gas exhaust capabilities that are currently provided by 3 turbomolecular pumps (TMPs) per divertor unit with an effective pumping speed of 3530 l/s at the pumping ports in the subdivertor [13], 10 cryo-vacuum pumps have been installed in the 10 island divertor units [14–16] of Wendelstein 7-X [17] and were operated for the first time during the experimental campaign OP2.1 in 2022/2023.

2. Cryo-vacuum pumps in Wendelstein 7-X

In each of the ten divertor modules, a cryo-vacuum pump was installed behind the horizontal target modules of the divertor for the most recent campaign OP2.1. A divertor module of Wendelstein 7-X is shown in Fig. 1 and mainly consists of the low iota and high iota divertor section. Horizontal and vertical divertor targets absorb the heat load associated with the plasma in the scrape-off layer and the neutral particles forming at the divertor targets enter the subdivertor volume through the large or small pumping gap and are pumped from the subdivertor volume using turbomolecular pumps and cryo-vacuum pumps.

* Corresponding author.
E-mail address: victoria.haak@ipp.mpg.de (V. Haak).
[1] See author list of Thomas Sunn Pedersen et al. 2022.

https://doi.org/10.1016/j.fusengdes.2024.114671
Received 10 June 2024; Received in revised form 15 August 2024; Accepted 8 September 2024
Available online 11 September 2024

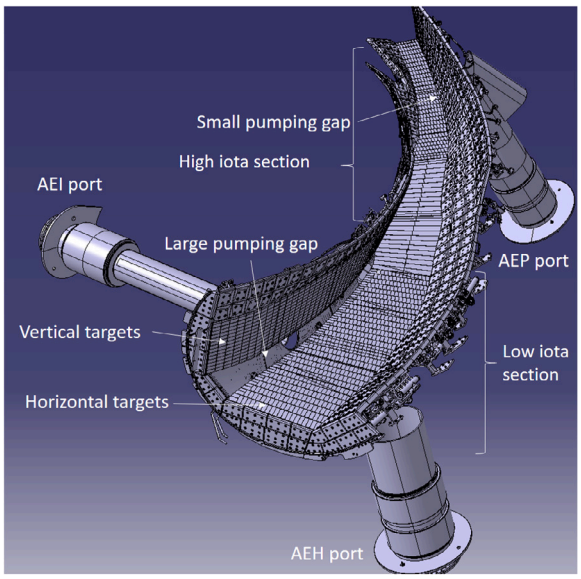

Fig. 1. Divertor module of Wendelstein 7-X consisting of the low and high iota divertor section, the large pumping gap, the vertical and horizontal divertor targets as well as the AEH, AEI and AEP ports connected to the subdivertor volume.

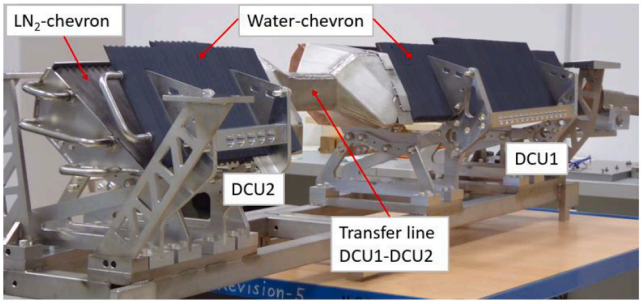

Fig. 2. The two units of a cryo-vacuum pump, i.e. DCU1 and DCU2, mounted on a temporary structure. Water-cooled and liquid nitrogen-cooled chevrons are used for thermal protection of the He-panels, which are located behind the LN_2-chevrons in this picture.

One of the cryo-vacuum pumps as installed in Wendelstein 7-X is shown in Fig. 2. To allow access through a port, the CVP is divided into two parts [18,19] i.e. DCU1 and DCU2, as shown in Fig. 2. The coolant to both these parts is provided in series. Cooling of the He-panels, liquid nitrogen (LN_2) cooled chevrons and water-cooled chevrons is provided using supercritical helium at ca. 4 K [20,21], liquid nitrogen at ca. 80 K [22,23] and cooling water at ca. 30° C, respectively. The water-cooled chevrons are coated with an Al_2O_3-TiO_2 layer to absorb the ECRH stray radiation to reduce the thermal loads on cryo-surfaces. A detailed thermo-mechanical analysis was performed using ANSYS to validate the operation of CVPs in the subdivertor environment [24]. The details of the construction of the CVPs are described in [25,26].

For design calculations, the pumping speed (S) of one CVP is given by [27,28] as

$$S = C \cdot A_{baffle} \cdot \frac{v}{4} = C \cdot A_{baffle} \cdot \sqrt{\frac{RT}{2\pi M}} \quad (1)$$

Here, C is the capture coefficient i.e. the probability of a particle passing through the baffle chevrons and being captured by the cryo-surface, A_{baffle} is the cross section of the baffle area through which the particle passes through (=1.957 m^2 for 10 CVPs), v is the mean thermal velocity of the particles with a Maxwell velocity distribution, R is the universal gas constant, T is the temperature of the gas entering the pump through the chevrons, which is assumed to be equivalent to the temperature of the surroundings i.e. the plasma vessel (25° C) and M is the molecular mass of hydrogen. The cryo-surface is composed of helium-cooled pipes, for which the capture coefficient under the assumption of one-sided pumping and equal surface areas of both baffles is given by

$$\frac{1}{C} = \frac{l}{\alpha \cdot d} + \frac{1}{w_1} + \frac{1}{w_2} - 2 \quad (2)$$

according to [27, p. 38 and following pages], [28]. The second and the third term on the right-hand side represent the probabilities of a particle passing the water- and the LN_2-cooled chevron and the first term represents the probability of the particle hitting one of the helium-pipes. In Eq. (2), d = 12 mm is the diameter of the helium pipes, l = 21 mm is the distance between the centers of two adjacent helium pipes, w_1 and w_2 are the transmission probabilities of the particles passing through the water-cooled and LN_2-cooled chevrons which are taken as 0.22 according to Monte-Carlo simulations presented in [27, p. 25], [28] (for Φ = 45° and A/B = 2). α is the sticking probability of the hydrogen molecules on the cryo-surface, which depends on multiple factors such as the gas type, gas temperature, the structure of the adsorbing surface and the surface temperature [27,28]. Literature data for the sticking coefficient is scarce, but values between 0.6 and 1 can be found for hydrogen at gas and cryo-surface temperatures corresponding to the ones of the CVPs in W7-X [27, p. 60], [11,28] and are subject to considerable uncertainty. Therefore, the pumping speed is given for α ranging from 0.6 to 0.8 and the estimated pumping speed of 10 CVPs in front of the water chevrons is 86 - 93 $\frac{m^3}{s}$. In the following sections, the pumping speed given for the CVPs always refers to the ensemble of 10 individual cryo-vacuum pumps.

3. Characterization of the cryo-vacuum pump

In a series of tests in which a known amount of hydrogen gas was injected into the plasma vessel, the pumping capacity of the CVPs was determined and used to validate a time-dependent conductance model for the neutral gas pressures in the plasma vessel and the subdivertor under the influence of cryo-vacuum pumping. For the pumping capacity tests, a known rate of hydrogen gas was injected in three divertor modules of W7-X after cooling down all ten CVPs and stabilizing the temperatures. The amount of gas injected for the tests is given in mbar m^3/s under the assumption that the temperature of the gas remains constant at 25° C. The common supply and return temperatures are <3.85 K and <4.10 K for the He-panels and <90 K and <79 K for the LN2-cooled chevrons. These temperatures were measured in a valve box located approximately 10 m away from the W7-X cryostat. The LN2-cooled chevrons are cooled with subcooled or saturated nitrogen at a pressure of 0.4–0.5 MPa. The mass flow is adjusted with a common control valve in the return line, which causes cooling of the returning liquid nitrogen due to expansion. The actual temperatures in the CVPs are not measured, but are expected to be lower than the measured return temperatures. The valves to the mechanical plasma vessel pumping system (i.e. turbo-molecular pumps) were closed to ensure pumping is only done by the CVPs. MKS Baratron and Piezo/Pirani pressure gauges installed in the pumping duct were used for the measurement of the neutral gas pressure in the subdivertor. As the baratron (type 627F.1MLD4B from MKS Instruments) measurements are temperature stabilized and gas type independent, pressure measurements from the baratrons at different locations around the torus were used to estimate the pumping speed of the CVPs. However, the pressure measurements from the twenty Piezo/Pirani gauges which are evenly distributed in the upper and lower parts around the torus are compared to check the uniformity of the neutral gas pressures throughout the plasma vessel to ensure that all CVPs have similar gas throughput conditions.

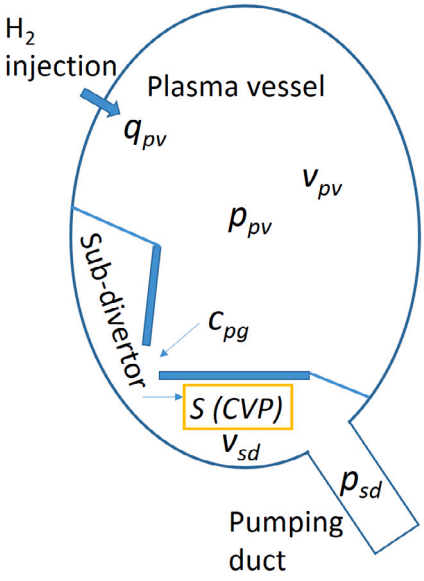

Fig. 3. Schematic diagram of the two chamber model consisting of the plasma vessel and the subdivertor region.

3.1. Two-chamber model

To understand the behaviour of the neutral particles inside the plasma vessel and subdivertor region under the aspect of optimized gas exhaust, a conductance model has been developed. It is based on the simplified representation of the pumping gap as a conductance between the plasma vessel and the subdivertor volume as shown in Fig. 3. The CVPs, which are installed behind the horizontal divertor modules act as a particle sink in the subdivertor volume, while the particle source is given by the gas inlet into the plasma vessel. Particle exchange between the plasma vessel and the subdivertor volume is limited by the conductance and thus the geometric properties of the pumping gap.

The full gas balance equations for the two chamber model are defined as:

$$\frac{dp_{pv}}{dt} = \frac{C_{pg}}{V_{pv} - V_{sd}} \cdot (p_{sd} - p_{pv}) + \frac{1}{V_{pv} - V_{sd}} \cdot (q_{pv} - q_{loss}) \tag{3}$$

$$\frac{dp_{sd}}{dt} = \frac{C_{pg}}{V_{sd}} \cdot (p_{pv} - p_{sd}) - p_{sd} \cdot \frac{S}{V_{sd}} \tag{4}$$

Here, p_{pv} and p_{sd} are the pressures during gas injection in the plasma vessel and the subdivertor, V_{pv} and V_{sd} the volumes of the plasma vessel and subdivertor region, respectively, C_{pg} is the conductance of the pumping gap, q_{pv} is the rate of hydrogen gas injection into the plasma vessel and q_{loss} is the loss rate e.g. retention by the plasma-facing components, which is difficult to quantify and is not considered here for simplicity. For the steady-state case with a constant pressure in the plasma vessel and the subdivertor region the equations reduce to:

$$0 = C_{pg} \cdot (p_{sd} - p_{pv}) + q_{pv} \tag{5}$$

$$0 = C_{pg} \cdot (p_{pv} - p_{sd}) - p_{sd} \cdot S \tag{6}$$

with

$$C_{pg} = A_{pg} \cdot \sqrt{\frac{RT}{2\pi M}} \tag{7}$$

Here, $A_{pg} = 0.1543\,m^2$ is the area of the pumping gap between the horizontal and vertical divertor modules and R is the universal gas constant. Using q_{pv} from Eq. (5) into Eq. (6), the pumping speed of the CVPs is:

$$S = \frac{q_{pv}}{p_{sd}}. \tag{8}$$

Table 1
Estimated pumping speed for all 10 cryo-vacuum pumping units, with $p_{sd,average}$ being the average neutral gas pressure of three baratrons installed in half-module 18, 29 and 49 in Wendelstein 7-X in the subdivertor region during the gas puff.

Gas puff	Injected H_2 q_{pv} [mbar m³/s]	$p_{sd,average}$ [mbar]	CVP pumping speed S [m³/s]
420 s pulse start	0.131	$1.87 \cdot 10^{-3}$	70
420 s pulse end	0.131	$1.90 \cdot 10^{-3}$	69
pulse 1	0.015	$2.11 \cdot 10^{-4}$	71
pulse 2	0.020	$2.82 \cdot 10^{-4}$	71

3.2. Experimental determination of the pumping speed

Several gas injection tests were performed for the experimental determination of the pumping speed of the CVPs. A long gas puff of 420 s was carried out with a total hydrogen gas injection rate of 0.131 mbar m³/s. The supply temperature for the freshly regenerated He-pipes was 3.83 K and the return temperature of 4.10 K stayed constant throughout the gas injection. A stable neutral gas pressure in the plasma vessel was achieved with a slight pressure increase of 1.5% from $1.87 \cdot 10^{-3}$ mbar to $1.9 \cdot 10^{-3}$ mbar from the beginning to the end of the long pulse. The estimated CVP pumping speed according to Eq. (8) slightly decreases from 70 to 69 m³/s throughout the discharge due to the formation of a layer of hydrogen on the cryo-surface. An overview of the neutral gas pressures during hydrogen gas injection, the injection rates and the estimated pumping speeds is given in Table 1. With a total injected amount of 55.02 mbar m³ of H_2 and a surface area of the He-pipes of all 10 CVPs of 2.67 m², the estimated thickness of the frozen hydrogen layer on the He-pipes is 21.6 μm when taking into account the density of H_2 of 0.09 kg/m³ at standard temperature and pressure and 86 kg/m³ for frozen H_2. The built-up of this H_2-layer results in a slight increase of the surface temperature and consequently a decrease of the pumping speed of the CVPs throughout operation.

Additionally, two shorter gas puffs with lower densities were evaluated with regard to the pumping speed of the CVPs and are shown in orange in Fig. 4. Hydrogen was injected at injection rates of 0.015 mbar m³/s (pulse 1) and 0.02 mbar m³/s (pulse 2) for a duration of about 20 s each. The temperature of the He-pipes stayed constant throughout the gas puffs and a supply temperature of 4.46 K and a return temperature of 4.61 K were measured. The measured values of the average pressures in the subdivertor region $p_{sd,average}$ are one order of magnitude lower than during the long gas puff and are shown in Table 1. The estimated CVP pumping speed according to Eq. (8) is 71 m³/s for both of the shorter gas puffs. To calculate the pumping speeds, the pressure at the end of the 20 s long gas puff was used. Using Eqs. (3), (4) and (7), the evolution of the neutral gas pressure in the subdivertor volume before, throughout and after the gas injection is modelled for both pulses and shown in black in Fig. 4. The zero offset that can be observed in the measurement of the neutral gas pressure during the experiment was corrected for the simulation. As shown in Fig. 4, a good agreement is found between the neutral gas pressure measurement during the experiment and the predicted evolution of the neutral gas pressure in the subdivertor.

The comparison of the CVP pumping speeds estimated by the three gas puffs shows that the value of the pumping speed is in the range of 70 ± 1 m³/s. Compared to the theoretical estimate of the pumping speed of 86–93 m³/s as presented in Section 2, the experimentally determined value is much lower, which could indicate that the sticking coefficient is lower than assumed for the calculations. A detailed overview of the regeneration of the CVPs is given in [29].

Although hydrogen (and later deuterium) is used for plasma operation and therefore is the main gas species that needs to be exhausted by the CVPs and other pumping systems, a variety of other gases is used during plasma operation too, e.g. for diagnostic purposes or for impurity seeding. Thus, a characterization of the pumping speed of the

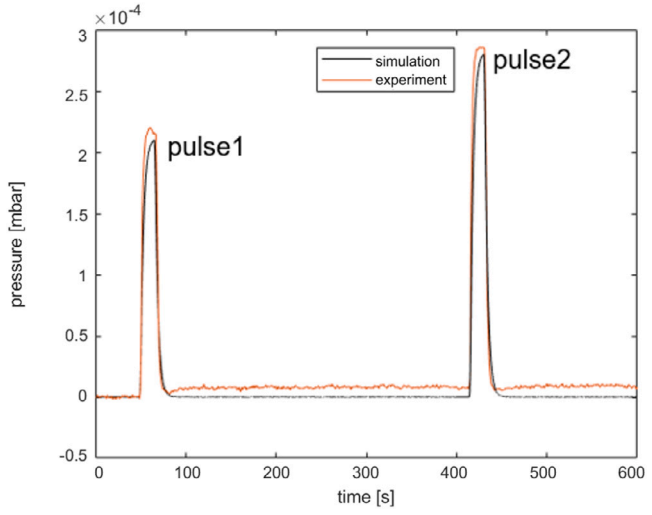

Fig. 4. Neutral gas pressure measured (orange) and calculated based on the two chamber model (black) in the subdivertor during hydrogen gas puffs of 15 and 20 mbar l/s.

CVPs with regard to those gas species is desirable and was attempted for nitrogen, neon and argon. The respective gases were injected into the plasma vessel with the CVPs used for pumping. The pumping speeds of the CVPs for the respective gases were derived from the gas puffs as described above and are shown in Table 2. The first value of the pumping speed corresponds to a supply temperature of the He-pipes of 4.48 K and a return temperature of 4.63 K and the second value was obtained at lower temperatures of the He-pipes of 3.83 K for the supply and 4.06 K for the return temperature.

A pumping speed of around 21 m^3/s for nitrogen, 22 m^3/s for neon and 9.4 m^3/s for argon was determined. However, due to the degeneration of the cryo-surface throughout the test despite the lower temperature of the cryo-surface for the second half of the test, the later measurements result in slightly lower pumping speeds, as can be seen in Table 2.

A significant factor for the lower pumping speed for these gases compared to hydrogen is the higher mass, leading to a lower conductance (see Eq. (7)) and therefore lower neutral gas pressure in the subdivertor volume at a given gas injection rate. The conductance for each gas relative to hydrogen C_{rel} is given in Table 2 as well as an estimate of the pumping speeds of the CVPs S_{es} based on the conductances and the pumping speed determined for hydrogen in Section 3.2:

$$S_{es} = \frac{C_{pg,gas}}{C_{pg,H2}} \cdot S_{H2} = \sqrt{\frac{M_{H2}}{M_{gas}}} \cdot S_{H2} \tag{9}$$

Except for the case of argon, in which the estimated pumping speed differs from the experimentally determined value by 66%, the estimated pumping speeds are in good agreement with the pumping speeds determined from the gas puffs. In the simple estimate made here, differences in the sticking coefficients that might exist for the different gases are not taken into account.

4. Neutral gas pressure and particle exhaust during plasma operation with the cryo-vacuum pump

During the previous campaign OP1.2b, the neutral gas pressures in the subdivertor region without CVPs were studied extensively in [13, 30–34]. Neutral gas pressure gauges are installed in several locations in the subdivertor, which can be divided into two main parts as shown in Fig. 1. The low iota subdivertor section includes the main subdivertor volume and exhibits high neutral gas pressures in the standard magnetic field configuration, when the strike line is near the large pumping gap. The CVPs are installed in the low iota subdivertor section as well as two TMPs. The smaller subdivertor volume, the so-called high iota subdivertor section shows high neutral gas pressures in the high iota magnetic field configuration, in which the strike line is located near the small pumping gap in the high iota subdivertor section. One TMP is installed in the high iota subdivertor section. A more detailed overview of the divertor geometry is given in [34].

Table 2
Experimentally determined (S) and estimated pumping speed (S_{es}) for all 10 cryo-vacuum pumping units for different gases; the results for hydrogen as presented in section 3.2 are listed for comparison.

Gas	Injection rate q_{pv} [mbar m^3/s]	Pumping speed S [m^3/s]	Estimated pumping speed S_{es} [m^3/s]
H_2	0.015 s for 20 s	71.0	71.0
H_2	0.020 for 20 s	71.0	
N_2	0.003 for 120 s	21.9	19.05
N_2	0.003 for 120 s	19.9	
Ne	0.003 for 120 s	22.2	22.44
Ne	0.003 for 120 s	21.6	
Ar	0.003 for 120 s	9.4	15.95
Ar	0.003 for 120 s	9.4	

Without the use of the CVPs during OP1.2b, the most frequently used standard magnetic field configuration resulted in neutral gas pressures of up to $3.5 \cdot 10^{-4}$ mbar in the low iota subdivertor section and $1.5 \cdot 10^{-4}$ mbar in the high iota subdivertor section at line integrated densities of $8 \cdot 10^{19}\ m^{-2}$. Higher neutral gas pressures were reached in the high iota magnetic field configuration with up to $1 \cdot 10^{-3}$ mbar in the high iota subdivertor section and $1 \cdot 10^{-4}$ mbar in the low iota subdivertor section at line integrated densities of $10 \cdot 10^{19}\ m^{-2}$ and without cryo-vacuum pumping. Especially the high iota subdivertor section has proven more favorable for particle exhaust as relatively high neutral gas pressures were obtained in this region in both, standard and high iota magnetic field configuration [34].

For the recent campaign OP2.1, the CVPs were installed behind the horizontal divertor modules in the low iota subdivertor section, leading to geometric modifications of the subdivertor space. Additionally, divertor closure plates separating the low iota subdivertor volume from the high iota subdivertor volume were removed for OP2.1, leading to a more homogeneous neutral gas pressure distribution in the subdivertor volume. Plasma operation was carried out with and without the CVPs in operation for different magnetic field configurations.

Fig. 5 shows the neutral gas pressures in the different parts of the subdivertor and the midplane obtained in OP2.1 with (blue) and without (red) the CVPs in operation for the standard magnetic field configuration. The error of the neutral gas pressure measurements is assumed to be 15% [35].

Without the CVPs in operation, the neutral gas pressures in the standard configuration of up to $1 \cdot 10^{-4}$ mbar in the low iota subdivertor section and $4 \cdot 10^{-5}$ mbar in the high iota subdivertor section at line integrated electron densities of $8 \cdot 10^{19}\ m^{-2}$ are about a factor of 3 lower than in the previous campaign OP1.2b, likely due to the missing divertor closure plate that was removed from the subdivertor for OP2.1. Consequently, the particles entering through the large pumping gap into the low iota subdivertor section in the standard configuration and through the small pumping gap into the high iota subdivertor section in the high iota configuration now occupy the whole subdivertor volume instead of only the low or high iota subdivertor section as previously, leading to lower neutral gas pressures.

When comparing the neutral gas pressure in the midplane to the neutral gas pressure in the subdivertor volume, compression ratios ranging from 2 to 61 and with a mean value of 18 were obtained for the discharges in standard configuration for the low iota subdivertor section. For the high iota configuration as shown in Fig. 6, the compression ratios range from 1 to 54 with a mean value of 16 for the high iota subdivertor section. For both the standard and the high

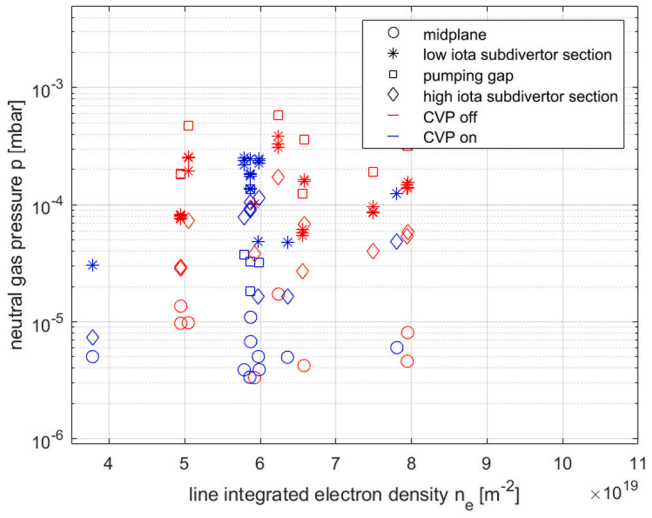

Fig. 5. Average neutral gas pressure in the midplane, low iota subdivertor section, near the pumping gap and in the high iota subdivertor section with respect to the line integrated electron density during plasma operation with (blue data points) and without (red data points) the cryo-vacuum pumps in the standard magnetic field configuration.

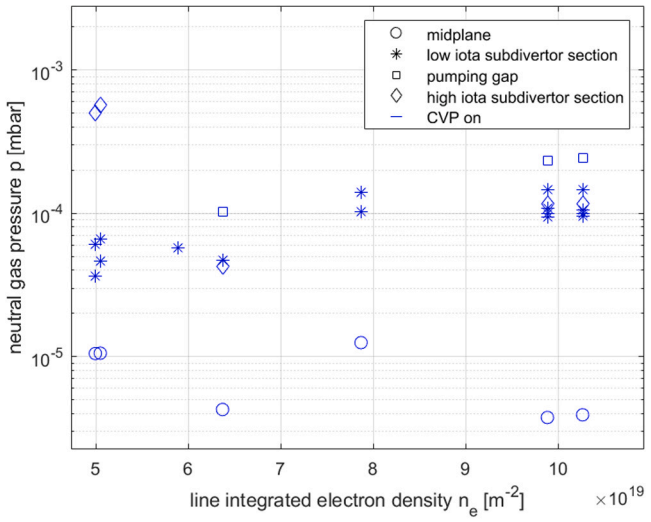

Fig. 6. Average neutral gas pressure in the midplane, low iota subdivertor section, near the pumping gap and in the high iota subdivertor section with respect to the line integrated electron density during plasma operation with the cryo-vacuum pumps in operation in the high iota magnetic field configuration.

iota configuration, those values are lower than the ones obtained in OP1.2b [34], which is likely also due to the removal of the separation plates between the low and high iota subdivertor volume.

In the high iota magnetic field configuration, a comparison to the previous campaign is not possible, because no plasma discharges without the CVPs were performed (see Fig. 6). However, the comparison of plasma discharges with and without the CVPs as shown in Fig. 5 indicates that the CVPs do not have a significant impact on the neutral gas pressures in the subdivertor. The neutral gas pressures obtained in W7-X in the recent campaign correspond to the molecular flow regime, in which particle exhaust by the CVPs is limited due to the low particle flux towards the cryo-surfaces.

This is not the case in many other plasma experiments that are able to reach higher neutral gas pressures. Subdivertor neutral gas pressures of 6 $\cdot 10^{-2}$ mbar were obtained in the ASDEX-Upgrade tokamak [36], 5 $\cdot 10^{-2}$ mbar in JET [37], 4 $\cdot 10^{-2}$ - 8 $\cdot 10^{-2}$ mbar in Alcator C-Mod [38,39] and 1 $\cdot 10^{-3}$ mbar in EAST [40,41]. In the stellarator Wendelstein 7-AS, neutral gas pressures of 5 $\cdot 10^{-3}$ mbar were measured [42], which is three times higher than the maximum neutral gas pressure of 1.75 $\cdot 10^{-3}$ mbar reached in Wendelstein 7-X [34]. An even higher neutral gas pressure of 1.4 $\cdot 10^{-2}$ mbar was recently measured in the Large Helical Device [43], in which effective density control by cryo-vacuum pumping could also be demonstrated [9]. Besides the installed pumping capacity in a given device, the neutral gas pressure in the subdivertor is the main factor determining particle exhaust. To reach the goal of effective density control by particle exhaust in Wendelstein 7-X, the particle exhaust rates and thus the subdivertor neutral gas pressure need to be increased. In order to obtain higher plasma densities at the divertor targets leading to higher neutral gas pressures in the subdivertor, the separatrix density needs to be increased [44], which will be addressed in the upcoming experimental campaigns of Wendelstein 7-X.

The neutral gas pressure in the subdivertor determines the flow regime, which will transition from the molecular to the continuous flow regime with increasing neutral gas pressures. The conductance of the subdivertor volume that connects the pumping gap to the different pumping systems is dependent on the flow regime present in the subdivertor and increases with increasing pressure in the continuous flow regime [45]. Thus, a higher effective pumping speed at the pumping gap resulting from cryo-vacuum pumping will lead to increased particle exhaust at neutral gas pressures above the molecular flow regime.

5. Simulation and validation

A fraction of the neutral particles generated at the strike lines during plasma operation enters the subdivertor region via the pumping gap, and is then pumped by the cryo-vacuum and turbo-molecular pumps. The neutral particle flux for a given plasma configuration is estimated by the EMC3-EIRENE code. The incoming particle flux together with the effective pumping capacities in the subdivertor region determine the pressures and consequently the flow regime i.e. molecular flow regime, transition flow regime or viscous flow regime in the subdivertor region. The pressure profiles in this region are simulated using ANSYS and the DIVGAS code.

5.1. Simulations of the neutral gas pressure in the molecular flow regime in ANSYS

Finite element simulations in ANSYS were carried out to study the distribution of the neutral gas pressure in the subdivertor volume under the influence of the CVPs. Since the molecular flow regime is dominant for the neutral gas pressures obtained in the subdivertor of W7-X, the steady-state thermal package in ANSYS can be adapted to model the behaviour of the neutral gas particles. A more detailed explanation of the method is given in [34].

A simulation was carried out for a particle flux of 10^{21} particles/s through the large pumping gap. The results are shown in Fig. 7 and indicate a neutral gas pressure of about $2 \cdot 10^{-4}$ mbar near the low iota side of the subdivertor volume. At a pressure of $1.5 \cdot 10^{-4}$ mbar as measured by the neutral gas pressure gauges in the subdivertor volume during discharges with similar particle flux into the subdivertor volume, the mean free path of hydrogen molecules at room temperature (300 K) corresponds to 0.84 m, which is of the order of the characteristic length of the subdivertor structures, indicating that the approach based on the assumption of a molecular flow regime is valid at these pressures.

5.2. Monte-Carlo simulations using DIVGAS

A more sophisticated approach to modelling the particle exhaust in the subdivertor region is based on the DIVGAS code, a direct simulation Monte Carlo method covering the entire neutral gas pressure regime in the subdivertor. DIVGAS has already been used to model the exhaust in other fusion devices like JET [46] and has now been applied to

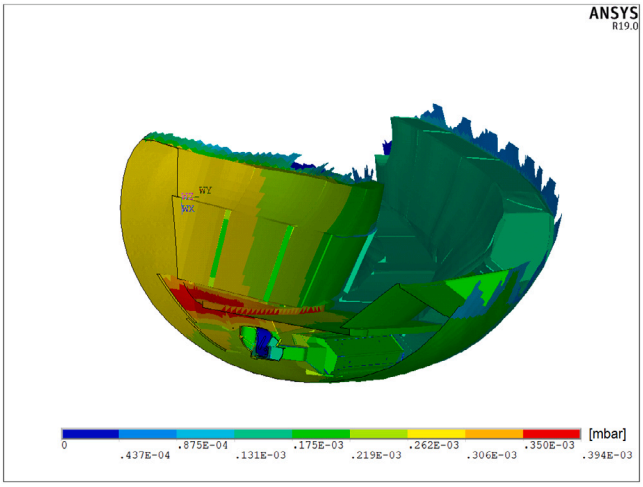

Fig. 7. ANSYS simulation results showing the pressure distribution in the subdivertor region.

Table 3
Comparison of the neutral gas pressures calculated for the low iota subdivertor volume using DIVGAS and ANSYS simulations with a particle flux of 10^{21} particles/s through the large pumping gap as well as neutral gas pressures measured at the AEH port in the low iota subdivertor section during plasma discharges in standard magnetic field configuration with a heating power of 3 MW and a line integrated electron density of $7{\cdot}10^{19}\,m^{-2}$.

	Neutral gas pressure in subdivertor with CVPs & TMPs on [mbar]	Neutral gas pressure in subdivertor with CVPs off & TMPs on [mbar]
DIVGAS	$1.5{\cdot}10^{-4}$	$1.8{\cdot}10^{-4}$
ANSYS measured in low iota subdivertor volume	$2{\cdot}10^{-4}$ $4{\cdot}10^{-5}$–$1.5{\cdot}10^{-4}$	– $5{\cdot}10^{-5}$–$3{\cdot}10^{-4}$

Wendelstein 7-X [47]. The code takes into account the complex 3D geometry of the subdivertor region of W7-X including the CVPs and performs the simulations in a wide range of Knudsen numbers i.e. from collisionless molecular flow to near viscous flow. As boundary condition towards the plasma the incoming particle flux to the pumping gap was varied in a parametric manner. It was found that the openings between individual components of the divertor result in a significant amount of particles leaking back from the subdivertor volume into the plasma vessel. Additionally, components in the subdivertor volume reflect a fraction of the particle flux entering the subdivertor volume back towards the plasma vessel through the large pumping gap. Consequently, a significant portion of the incoming particle flux cannot be exhausted by the pumps [47].

Simulations were performed for an incoming particle flux of 10^{21} particles/s through the large pumping gap into the low iota section of the subdivertor and 10^{20} particles/s through the small pumping gap into the high iota section of the subdivertor. EMC3-EIRENE analysis suggests that a neutral particle flux of the order of 10^{21} particles/s is expected for the standard configuration in a plasma discharge with a line-integrated density of $7{\cdot}10^{19}\,m^{-2}$ and a heating power of 3 MW [48]. For these particle fluxes, the DIVGAS simulations show estimated neutral gas pressures of about $1.5 \cdot 10^{-4}$ mbar for the case with CVPs and TMPs on and about $1.8 \cdot 10^{-4}$ mbar for CVPs off and TMPs on. A comparison of the results from the DIVGAS and ANSYS simulations is given in Table 3 together with experimental data.

The neutral gas pressures calculated using DIVGAS are comparable to the measured neutral gas pressures in the low iota section of the subdivertor region of $4 \cdot 10^{-5}$ mbar - $1.5 \cdot 10^{-4}$ mbar and $5 \cdot 10^{-5}$ mbar - $3 \cdot 10^{-4}$ mbar for the discharges with and without CVPs in operation (TMPs on in both cases), respectively. This shows that the DIVGAS simulations are in agreement with the actual plasma experiments at the mentioned plasma parameters in the standard magnetic field configuration.

6. Conclusions and outlook

During the recent OP2.1 plasma campaign at Wendelstein 7-X, the cryo-vacuum pumps were successfully operated for the first time. The hydrogen retention capabilities of the CVPs were sufficient to maintain plasma operation without regeneration of the CVPs during the week. The He-pipes and LN_2-cooled chevrons of the CVPs were regenerated after each weekly operation. Dedicated hydrogen gas injection tests revealed a pumping speed of $70 \pm 1\ \frac{m^3}{s}$. This value is lower than the theoretical value of 86–93 $\frac{m^3}{s}$ for sticking coefficients between 0.6 and 0.8 based on a conductance approach, which is subject to uncertainties of the sticking coefficient and the transmission probabilities. The actual temperature distribution inside the He-pipes of the CVPs likely also deviates from the assumption of a homogeneous temperature of the cryo-surfaces.

According to the differences in mass, lower pumping speeds of the CVPs for other gases than hydrogen were determined, i.e. $21\,m^3/s$ for nitrogen, $22\,m^3/s$ for neon and $9.4\,m^3/s$ for argon.

During plasma operation, the neutral gas pressures in the subdivertor region were in the range of $3 \cdot 10^{-5}$ mbar - $5 \cdot 10^{-4}$ mbar and therefore lower than in the previous campaign. At these low neutral gas pressures in the subdivertor, the particle exhaust through the CVPs is limited due to the molecular particle flow. The ANSYS simulations based on the assumption of collisionless molecular particle flow and DIVGAS simulations that take into account neutral-neutral collisions show an acceptable agreement in terms of neutral gas pressure, given the imposed free molecular conditions as well as the desired level of accuracy (≈15%). In the case of higher subdivertor neutral gas pressures, in which the neutral-neutral collisions dominate the particle dynamics, the free molecular approach is not valid anymore and reliable simulations can only be achieved using DIVGAS. Studies of the neutral particle fluxes and exhaust processes at higher neutral gas pressures using DIVGAS are currently ongoing.

CRediT authorship contribution statement

V. Haak: Writing – review & editing, Writing – original draft, Visualization, Methodology, Formal analysis, Data curation, Conceptualization. **C.P. Dhard:** Conceptualization. **D. Boeyaert:** Formal analysis. **T. Bräuer:** Methodology, Investigation. **V. Bykov:** Formal analysis. **C. Day:** Investigation. **S. Degenkolbe:** Resources. **G. Ehrke:** Resources. **J. Igitkhanov:** Investigation. **M. Khokhlov:** Formal analysis. **T. Kremeyer:** Methodology, Investigation. **M. Nagel:** Resources. **D. Naujoks:** Supervision. **M. Pietsch:** Resources. **D. Pilopp:** Resources. **G. Schlisio:** Data curation. **H. Strobel:** Methodology, Investigation. **C. Tantos:** Methodology, Investigation. **S. Varoutis:** Methodology, Investigation. **H. Viebke:** Resources. **O. Volzke:** Resources.

Declaration of competing interest

The authors declare that they have no known competing financial interests or personal relationships that could have appeared to influence the work reported in this paper.

Data availability

Data will be made available on request.

Acknowledgements

This work has been carried out within the framework of the EUROfusion Consortium, funded by the European Union via the Euratom Research and Training Programme (Grant Agreement No 101052200 - EUROfusion). Views and opinions expressed are however those of the author(s) only and do not necessarily reflect those of the European Union or the European Commission. Neither the European Union nor the European Commission can be held responsible for them.

The work of Dieter Boeyaert was funded by the U.S. Department of Energy under grant number DE-SC0014210.

References

[1] B. Streibl, et al., In-vessel cryo pump for ASDEX upgrade divertor II, Fusion Technol. (1997) 427.
[2] B. Streibl, et al., Operational behaviour of the ASDEX upgrade in-vessel cryo pump, Fusion Eng. Des. 56 (2001) 867.
[3] B. Streibl, et al., Hydrogen frosting scenarios with the ASDEX upgrade in-vessel cryo pump, Fusion Eng. Des. 69 (1–4) (2003) 103.
[4] G. Schall, et al., Design and operation of the in-vessel cryopump for the new upper divertor in ASDEX upgrade, Fusion Eng. Des. 166 (2021) 112316.
[5] W. Obert, et al., Performance of the JET pumped divertor cryopump system, in: Proceedings of 16th International Symposium on Fusion Engineering, Vol. 1, IEEE, 1995, p. 742.
[6] J.P. Smith, et al., The Design and Fabrication of a Toroidally Continuous Cryocondensation Pump for the DIII-D Advanced Divertor, Tech. rep, General Atomics, San Diego, CA (United States, 1991.
[7] H.J. Lee, et al., Design and fabrication of the KSTAR in-vessel cryo-pump, Fusion Eng. Des. 86 (9-11) (2011) 1993.
[8] Q.S. Hu, et al., The first in-vessel cryopump for EAST divertor experiment, Fusion Eng. Des. 85 (7–9) (2010) 1508.
[9] G. Motojima, et al., New approach to the control of particle recycling using divertor pumping in the large helical device, Nucl. Fusion 59 (2019) 086022.
[10] T. Murase, et al., Development of new concept in-vessel cryo-sorption pump for LHD closed helical divertor, Plasma Fusion Res. 11 (2016) 1205030.
[11] C. Day, et al., R & D and design for the cryogenic and mechanical vacuum pumping systems of ITER, Vacuum 81 (6) (2007) 738.
[12] C. Day, et al., Design progress for the ITER torus and neutral beam cryopumps, Fusion Eng. Des. 86 (9-11) (2011) 2188.
[13] U. Wenzel, et al., Gas exhaust in the Wendelstein 7-X stellarator during the first divertor operation, Nucl. Fusion 57 (11) (2022) 096016.
[14] Y. Feng, et al., Physics of island divertors as highlighted by example of W7-AS, Nucl. Fusion 46 (2006) 807.
[15] R. König, et al., The divertor program in stellarators, Plasma Phys. Control. Fusion 44 (2002) 2365.
[16] H. Renner, et al., Divertor concept for the W7-X stellarator and mode of operation, Plasma Phys. Control. Fusion 44 (6) (2002) 1005.
[17] T.S. Pedersen, et al., Experimental confirmation of efficient island divertor operation and successful neoclassical transport optimization in Wendelstein 7-X, Nucl. Fusion 62 (4) (2022) 042022.
[18] B. Streibl, C. Li, Ringbuch Kryopumpe, Tech. rep., 1-ACF-R0002.0. IPP internal report, 2013.
[19] G. Ehrke, et al., Design and manufacturing of the Wendelstein 7-X cryo-vacuum pump, Fusion Eng. Des. 146 (2019) 2757.
[20] M. Chorowski, et al., Proceedings, 23rd International Cryogenic Engineering Conference and International Cryogenic Materials Conference 2010, ICEC 23 - ICMC 2010, Wroclaw, Poland, (2010) 19-23, Wroclaw University of Technology, 2011, p. 531.
[21] C.P. Dhard, et al., Final acceptance tests of helium refrigerator for Wendelstein 7-X, Physics Procedia 67 (2015) 83.
[22] M. Nagel, et al., Concept for the cryo distribution for the Wendelstein 7-X cryo vacuum pumps, in: IOP Conference Series: Materials Science and Engineering, Vol. 502. 1, IOP Publishing, 2019, 012109.
[23] C.P. Dhard, S. Raatz, Cooling scheme for W7-X divertor cryo-vacuum pumps, Fusion Eng. Des. 86 (9–11) (2011) 2117.
[24] Z. Wang, et al., Thermal and mechanical analysis of the wendelstein7-X cryo-vacuum pump plug-in, IEEE Trans. Plasma Sci. 46 (5) (2017) 1576.
[25] J. Zhu, et al., Refined multiphysics analysis of W7-X cryopumps, IEEE Trans. Plasma Sci. 46 (5) (2018) 1592.
[26] S. Benhard, et al., Manufacturing of the Wendelstein 7-X divertor and wall protection, Fusion Eng. Des. 75 (2005) 463.
[27] R.A. Haefer, Kryo-Vakuumtechnik, Springer, 1981.
[28] R.A. Haefer, 1989, Cryopumping. Theory and practice. Monographies on Cryogenics.
[29] T. Bräuer, et al., First experiences of the new cryo vacuum pumps at Wendelstein 7-X during hydrogen operation, in: 15th International Symposium on Fusion Nuclear Technology, ISFNT-15, 2023.
[30] H. Grote, et al., Neutral particle modelling and particle exhaust in the Wendelstein 7-X stellarator, J. Nucl. Mater. 313 (2003).
[31] O. Schmitz, et al., Stable heat and particle flux detachment with efficient particle exhaust in the island divertor of Wendelstein 7-X, Nucl. Fusion 61 (2021) 016026.
[32] G. Schlisio, et al., The evolution of the bound particle reservoir in Wendelstein 7-X and its influence on plasma control, Nucl. Fusion 61 (3) (2021) 036031.
[33] T. Kremeyer, et al., Analysis of hydrogen fueling recycling, and confinement at Wendelstein 7-X via a single-reservoir particle balance, Nucl. Fusion 62 (3) (2022) 036023.
[34] V. Haak, et al., Overview over the neutral gas pressures in Wendelstein 7-X during divertor operation under boronized wall conditions, Plasma Phys. Control. Fusion 65 (5) (2023) 055024.
[35] U. Wenzel, et al., Performance of new crystal cathode pressure gauges for long-pulse operation in the Wendelstein 7-X stellarator, Rev. Sci. Instrum. 90 (2019) 123507.
[36] A. Kallenbach, et al., Neutral pressure and separatrix density related models for seed impurity divertor radiation in ASDEX upgrade, Nucl. Mater. Energy 18 (2019) 166.
[37] M. Groth, et al., Impact of carbon and tungsten as divertor materials on the scrape-off layer conditions in JET, Nucl. Fusion 53 (9) (2013) 093016.
[38] A. Niemczewski, et al., Neutral particle dynamics in the alcator C-mod tokamak, Nucl. Fusion 37 (2) (1997) 151.
[39] B. Lipschultz, et al., Neutrals Studies on Alcator C-Mod, MIT Plasma Science and Fusion Center, 2006.
[40] D. Zhou, et al., Measurement of divertor neutral pressure in EAST tokamak by ASDEX pressure gauge, Fusion Eng. Des. 196 (2023) 114024.
[41] N. Yan, et al., Dependence of upstream SOL density shoulder on divertor neutral pressure observed in L-mode and H-mode plasmas in the EAST superconducting tokamak, Nucl. Fusion 61 (7) (2021) 076018.
[42] M. Hirsch, et al., Major results from the stellarator Wendelstein 7-AS, Plasma Phys. Control. Fusion 50 (5) (2008) 053001.
[43] U. Wenzel, et al., Ultrahigh neutral pressures in the sub-divertor of the large helical device, Nucl. Fusion 64 (2024) 034002.
[44] Y. Feng, et al., Comparison between stellarator and tokamak divertor transport, Plasma Phys. Control. Fusion 53 (2011) 024009.
[45] Pfeiffer Vacuum, Conductance, 2024, url: https://www.pfeiffer-vacuum.com/en/know-how/introduction-to-vacuum-technology/fundamentals/conductance/.
[46] S. Varoutis, et al., Simulation of neutral gas flow in the JET sub-divertor, Fusion Eng. Des. 121 (2017) 13.
[47] S. Varoutis, et al., Numerical simulation of neutral gas dynamics in the W7-X sub-divertor, Nucl. Fusion 64 (2024) 076011.
[48] D. Boeyaert, et al., Analysis of the neutral fluxes in the divertor region of Wendelstein 7-X under attached and detached conditions using EMC3-EIRENE, Plasma Phys. Control. Fusion 66 (2024) 015005.